IX Australian Conference on Laser Diagnostics
Adelaide, Australia
December 2-4 2019

3D Accelerations of a Subsonic Jet using Four-Pulse Shake-The-Box

Peter Manovski[1], **M. Novara**[2], **N.K. Depuru Mohan**[3], **R. Geisler**[2], **D. Schanz**[2], **P. Godbersen**[2] **and A. Schröder**[2]

[1]Aerospace Division, Defence Science and Technology Group, VIC. 3207, AUSTRALIA
peter.manovski@dst.defence.gov.au
[2]Institute of Aerodynamics and Flow Technology, German Aerospace Centre (DLR), Göttingen D-37073, GERMANY
[3]University of Cambridge, Cambridge CB2 1PZ, UNITED KINGDOM

ABSTRACT

Three-dimensional (3D) Lagrangian Particle Tracking (LPT) was performed using the Shake-The-Box (STB) algorithm on a subsonic round jet flow at Mach 0.845. The STB technique for four-pulse data was employed to reconstruct particle tracks along the four-pulse sequences providing highly resolved 3D flow velocity and material acceleration data. A description of the experimental methodology is given followed by instantaneous accelerations and averaged flow statistics.

1. INTRODUCTION

Dual-plane or four-pulse Particle Image Velocimetry (PIV) methods provide increased accuracy and dynamic range as well as out-of-plane velocity gradients and accelerations to be determined. Kähler and Kompenhans [2] used this approach with the flow field illuminated by orthogonally opposed polarised light from four lasers to avoid multiple exposed particle images. This study was followed by Perret *et al.* [5], who measured the 3 components of acceleration using dual-plane Stereo-PIV. More recently the approach was extended to 3D with four-pulse Tomographic-PIV using two independent imaging systems (each with 4 cameras) [7]. In this paper a similar approach was used with four-pulse Shake-The-Box (STB). STB for time-resolved (TR) applications is described in Schanz *et al.* [6] and allows for accurate 3D LPT of densely seeded (>0.05 particles per pixel, ppp) flows however due to current limitations of camera and illumination hardware it is typically limited to low speed flows <10-20 m/s in air. Novara *et al.* [4] showed that a short time sequence (or multi-pulse) implementation of STB was able to retrieve most particle tracks with dynamic velocity and acceleration ranges comparable to those obtained with TR-STB, and they suggested the method can be used to measure the material acceleration for high-speed flows.

Jet flows and their radiated noise are classical fluid mechanics and aeroacoustic research topics that remain of high interest. The application of STB in jet aeroacoustics provides an accurate means of establishing a direct correlation between the flow dynamics in the jet near field and the acoustics pressure fluctuations in the far field. Ultimately, the pressure in the near field is the desired quantity to determine the sources of aeroacoustic noise and was a prime motivation for this study. The pressure field can be indirectly obtained via non-intrusive optical flow measurements of the material acceleration by PIV [9]. The pressure is obtained by spatial integration of the momentum equation and for turbulent flows at high Reynolds number, the viscous term has been shown to be negligible leaving the material acceleration to dominate and thus the most important measurement quantity [9]. In a more recent paper by van Gent *et al.* [8], a comparison of a range of techniques for pressure reconstruction showed that the accuracy can be significantly improved by using STB where the material acceleration is obtained directly from individual particle trajectories. The accuracy from PIV and STB for both time-resolved (TR) and multi-pulse input data was assessed. The TR-STB showed the lowest global error, the next best was four-pulse STB (1.6×larger error) followed by TR PIV and two-pulse PIV which showed higher errors (2× and 4×, respectively). This positive outcome for four-pulse STB has provided further motivation in the current study to measure the material acceleration with this method.

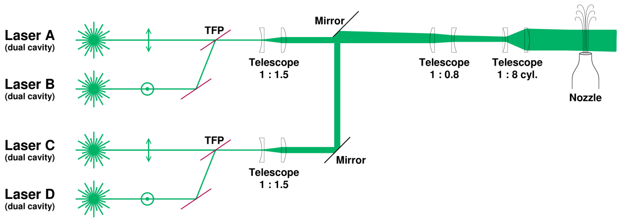

Figure 1: Laser illumination set-up consisting of four dual cavity lasers (A-D). TFP: Thin Film Polariser. Vertically polarised light (↕) and horizontally polarised light (⊙).

2. EXPERIMENTAL SET-UP

The experiment was carried out in the anechoic aeroacoustics test facility at the German Aerospace Center (DLR) Göttingen. A jet flow with Mach number (M) of 0.845, issued from a round nozzle with a diameter, D_j, of 15 mm and nozzle lip thickness of 3 mm was investigated. The nozzle pressure and temperature ratios were 1.72 and 0.98, respectively.

A four-pulse set-up was obtained by the combination of two dual-frame acquisition systems used to record particle images within a volume of $90\times70\times8$ mm^3 along the jet axial (x), radial (y) and out-of-plane (z) directions, respectively. The four-pulse acquisition strategy described by Novara *et al*. [3] is applied here, where the use of two different states of polarisation for the laser separates pulses on the camera frames. Illumination is provided by two dual-cavity Quantel Evergreen Nd:YAG lasers and two dual-cavity Big Sky Nd:YAG lasers (each with 200 mJ pulse energy at 10 Hz). Each laser pulse was combined with another resulting in a total energy per pulse of 400 mJ. The laser sheet was back reflected with a flat mirror to increase the illumination intensity of particles and to provide a more even particle imaging for both camera systems. The layout of the four dual-cavity lasers is shown in Fig. 1, as well as the optical arrangement used to produce the volumetric light sheet at the nozzle.

For the four-pulse sequence, the time separation between pulses 1 and 2, and that between pulses 3 and 4, is kept the same (1.25μs) and a longer time separates pulses 2 and 3 (3.75μs). The motivation for this pulse separation is to increase the velocity and acceleration dynamic range. The two imaging systems consisting each of four sCMOS PCO-Edge cameras, are equipped with polarisation filters to separate the four pulses onto the image sensor, and are shown in Fig. 2. One imaging system (odd camera numbers in Fig. 2) records pulses 1 and 2

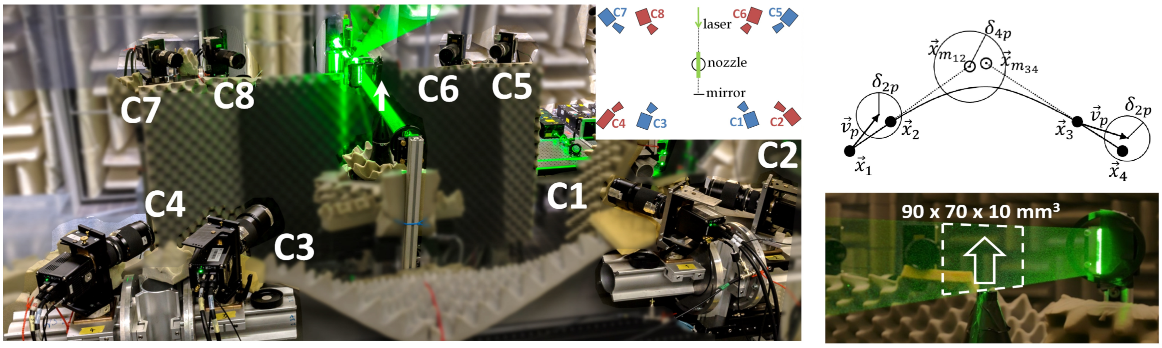

Figure 2: Left: in-line camera STB set-up with two imaging systems separated by two states of polarisation (indicated by the odd and even camera numbers). Top right: particle tracking strategy for uneven pulse separation. Bottom right: jet flow measurement volume.

and the other (even camera numbers), pulses 3 and 4. Cameras, in Scheimpflug condition, are equipped with lenses having a focal lengths of f = 200 and 180 mm. The digital resolution was 33.63 pixel/mm. The maximum displacement of particle tracers was 13 pixel and 39 pixel for the shorter and longer time interval respectively, resulting in a total particle shift of 65 px.

An aerosol generator was used to provide seeding of Di-Ethyl-Hexyl-Sebacat (DEHS) with a nominal particle diameter of 1 μm. The seeding was introduced upstream of the nozzle and the ambient air was also seeded enabling near homogeneous distribution across the measurement. The seeding resulted in a particle image density of approximately 0.015-0.04 *ppp*. The 3D imaging systems are calibrated using a LaVision two-plane target; volume self-calibration is used to compensate for calibration errors and to obtain the Optical Transfer Function of the particle images [3]. A total of 60,000 four-pulse sequences were recorded at 10 Hz.

2.1 Lagrangian Particle Tracking with Shake-The-Box

An adapted version of the STB 3D LPT algorithm, initially proposed by Schanz *et al*. [6] for time-resolved recordings, is applied here to four-pulse sequences. An iterative STB processing strategy is employed to compensate for the lack of a long observation time. The Iterative Particle Reconstruction technique (IPR, [10]) and the particle tracking procedure is briefly summarised in this section. A detailed description of the reconstruction and tracking strategy can be found in [4, 3]. Initially, the recorded images are reconstructed in 3D via IPR to triangulate and correct ('shake') particles for each of the four pulses. Next the particle matching procedure employed for the tracking phase is divided into two stages (with reference to Fig. 2 top right). At first, two-pulse tracks between pulses 1-2 and 3-4 are identified; around each particle in the first time step (pulse 1 and 3) a radius (δ_{2p}) is established to define a search area where matching particles from the second step (pulse 2 and 4) are identified. This step is aided by the use of instantaneous velocity predictors obtained by means of Particle Space Correlation (PSC, [4]) performed between IPR reconstructed particle fields ($\vec{v}_p$ in Fig. 2). The use of such a predictor allows for the reduction of the search radius thereby improving the identification of valid particle tracks [4]. The second stage of the tracking process is to obtain four-pulse tracks by connecting two-pulse tracks that have been identified. This is done by determining the position of the particles at the mid-point of the four-pulse sequence by extrapolating the two-pulse tracks from pulses 1-2 forward and 3-4 backward in time respectively ($\vec{x}_{m_{12}}$ and $\vec{x}_{m_{34}}$ in Fig. 2). A search radius δ_{4p} is established to define the area within which the predicted mid-points need to be found for the two-pulse tracks belonging to pulses 1-2 and 3-4 to be connected into four-pulse tracks. The search radii δ_{2p} and δ_{4p} are referred to as global radii; and their value is kept constant across the measurement domain. If an estimate of the velocity fluctuation components is available, the global search radii can be locally adapted according to the standard deviation of the velocity to obtain the local radii:

$$\delta^*_{2p} = \delta_{2p} + f_{\sigma,2p} \times \sigma, \quad \delta^*_{4p} = \delta_{4p} + f_{\sigma,4p} \times \sigma, \tag{1}$$

where σ indicates the standard deviation of the velocity in pixels and $f_{\sigma,2p}$ and $f_{\sigma,4p}$ are multiplicative factors that can be freely adjusted. Adaptive search radii enables an increase of the search area in regions where high flow dynamics are expected, therefore allowing the capture of high acceleration events.

After evaluation of the 4-pulse tracks is completed, a quadratic polynomial is used to fit the particle positions along the track and the average deviation from the fit is computed. If the deviation for a track is larger than a threshold value, the track candidate is discarded. Particles that could not be tracked over the complete four-pulse sequence are also rejected. This ensures that spurious ghost particles arising from the reconstruction process, typically not coherent with the flow motion, are discarded [4]. The chance of producing ghost tracks is further reduced by the use of two independent imaging systems [4]. After these steps, the retained particles are back-projected onto the image plane to form projected images; these are subtracted from the original recordings to obtain residual images. These steps constitute a single STB iteration; the images of particles which have not been reconstructed by IPR (e.g. due to particle image overlap) or failed to be matched during tracking (e.g. inadequate search radius) remain in the residual images. These residual images are then used to perform further STB iterations. The residual images have a lower particle image density, therefore offering a less complex reconstruction and tracking problem enabling the recovery of previously undetected tracks. For the first STB iteration lower values of the search radii and allowed deviation from fit are used to ensure that only the most reliable tracks are identified. After these particles have been subtracted from the recorded images, more challenging tracks (e.g. exhibiting higher noise or higher accelerations) can be identified by slowly relaxing the partner search and allowed deviation from fit. The particle velocity and acceleration are determined analytically from the quadratic fit, hence the double integration results in a constant acceleration over the four-pulse sequence. The midpoint position of the sequence is chosen for the evaluation from the fit as it provides the best accuracy.

For the present case, initially a batch of 200 four-pulse sequences were evaluated using the PSC method [4]. Then a batch of 10,000 were evaluated using STB and aided by a PSC mean field, as a predictor. The first STB averaged flow field results are then obtained by bin-averaging of the scattered 3D particle tracks into small volumetric bins as in [3]. The resulting bin-average was then used as a high fidelity predictor for the

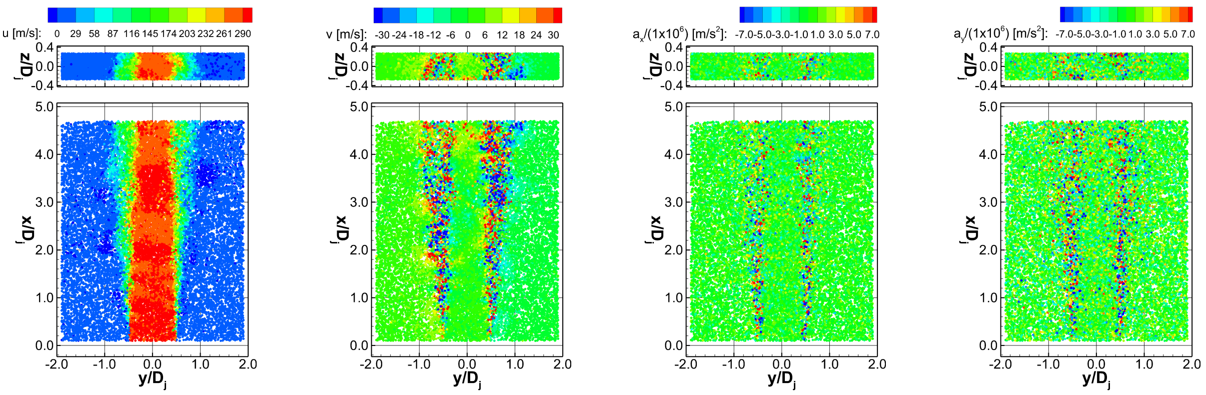

Figure 3: *M* 0.845 jet flow, instantaneous velocity and acceleration scatter plots of the axial and radial components.

STB evaluation of the total 60,000 sequences. For each of the four STB iterations the adaptive factors were progressively increased ($f_{\sigma,2p} = 2, 3, 4, 4$ px and $f_{\sigma,4p} = 4, 5, 6, 6$ px) ensuring that by the final (fourth) pass, events up to four times the local expected displacement standard deviation could be captured. As a result, an average of 30,000−50,000 tracks, depending on the seeding density and individual camera image quality, could be tracked for each sequence.

3. RESULTS

Experimental results are presented for the jet flow at *M* 0.845. Fig. 3 shows scatter plots of instantaneous four-pulse tracks colour-coded by the flow velocity and acceleration components. The number of tracked particles is approximately 35,000. The potential core region is clearly evident and extends past the measurement field. The jet shear layer is evident as regions of high radial velocity and acceleration. The layer is very thin near the nozzle exit, but quickly widens with increasing axial distance. Instantaneous accelerations greater than 7×10^6 m/s^2 are measured in the shear layer of the jet.

The mean acceleration flow field results are shown in Fig. 4 and are obtained by bin-averaging the scattered 3D particle track data into small bins. The bin size chosen here was 30 px, 10 px and 10 px (0.3 mm or $0.02 \cdot D_j$) in the axial (X), radial (Y) and out-of-plane (Z) directions, respectively. In order to resolve the high radial gradients in the shear layer smaller bin lengths were chosen whereas the lower velocity gradients in the axial direction allows the use of a larger bin length, thereby enabling more particle tracks to be collected. In Fig. 4 (top) the outer shear layer near the jet exit lip line ($y/D_j = 0.5$) shows the highest levels of acceleration, which represents the ambient flow that is entrained and accelerated by the fast jet core. Whereas, the highest levels of deceleration are in the inner shear layer as the jet flow in the core is decelerated within a very thin region at the nozzle exit, which broadens radially downstream. By $x/D_j \approx 3$, the axial acceleration levels subside to that of the ambient and jet core. The radial accelerations, Fig. 4 (middle) show in the inner shear layer, accelerations away from the potential core whereas the outer shear layer show accelerations towards the core that are broader and more diffuse. The fluctuations (standard deviation) of the particle axial accelerations are presented in Fig. 4 (bottom). Fluctuations in acceleration of up to 40 times greater than the maximum averaged values are evident.

Fig. 5 shows radial profiles of the normalised axial velocity (u/U_j) and fluctuations in the axial velocity (u'/U_j) and acceleration (a'_x/U_j^2) at $x/D_j = 0.2, 1, 4$. At locations, $1 \cdot D_j$ and $4 \cdot D_j$ the velocity profiles are compared with available data from [1] (*M* 0.9). Despite different flow conditions, the profiles of axial velocity compare well. At $1 \cdot D_j$ the benefit of the particle tracking approach over PIV (where the finite size of the cross-correlation windows results in a spatial averaging and modulation [6]) is highlighted by STBs ability in capturing the thin shear layer and the steep velocity gradients. The large sequence of recordings and the axial symmetry of the flow allowed cylindrical bins down to 0.75 px (23 μm or $0.0015 \cdot D_j$) in the radial direction and 20 px in the axial direction. In Fig. 5 (left), the axial velocity profile is shown at $0.2 \cdot D_j$ for 0.75 px and 10 px resolution. The step profile of the axial velocity is well captured with the 10 px resolution but is better resolved with 0.75 px bin size. The shear layer at this location is extremely thin as evident by the steep delta

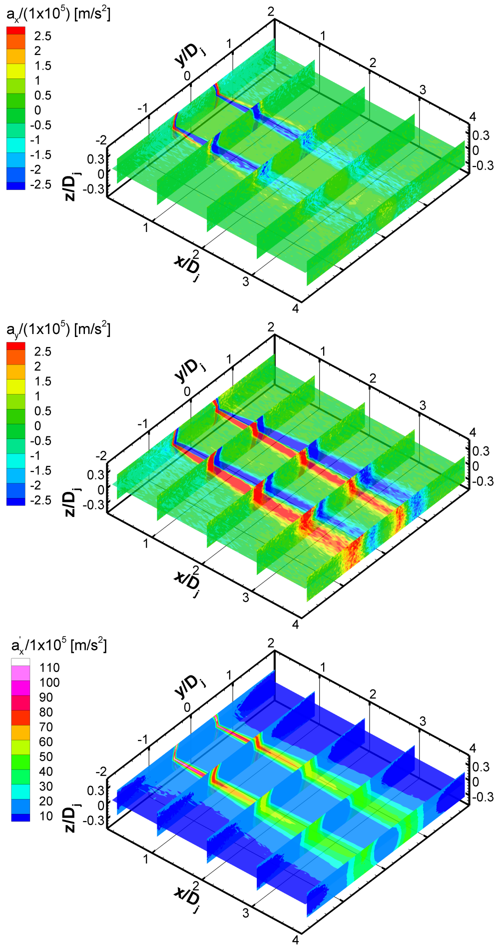

Figure 4: *M* 0.845 jet flow, (top) mean axial acceleration (a_x), (middle) radial acceleration (a_y) and (bottom) fluctuations of axial acceleration (a'_x). Streamwise slice at $z/D_j = 0$ and cross-stream slices at $x/D_j = 0.2, 1, 2, 3, 4$.

profile in the fluctuations (Fig. 5-right), and appear to be well resolved by STB. For a comparison, the size of a typical PIV correlation window of 32 px is indicated. The fluctuations in Fig. 5 (right) are scaled to match peak value at $0.2 \cdot D_j$. The profile shapes at $0.2 \cdot D_j$ compare well, however downstream the acceleration fluctuations decrease quicker compared to the velocity fluctuations.

Profiles of the dimensional bin-averaged axial and radial, velocity and acceleration components are shown in Fig. 6 at $x/D_j = 0.2$. The bin size here is 5 px ($0.01D_j$) and was selected to resolve the local flow features while ensuring statistical convergence. The velocity and subsequent acceleration response is shown with the number of samples (tracks) per bin on the left axis. Greater seeding was available in the jet core resulting in over 8,000 samples, however at the lip line where the accelerations are greatest there is a significant drop in the track count, down to 2,000. This drop was also observed in the bin-averaging of the IPR triangulated (without tracking) particles, indicating it is not due to a limitation of the tracking strategy. This behaviour was not observed in the downstream locations and therefore may be due to the local flow effects over the lip thickness or the particle lag of the tracer in regions of very high accelerations.

Fig. 7 shows the probability density function (PDF) of the non-dimensional axial, radial and out-of-plane particle accelerations. The PDFs are obtained from cylindrical bin averaging with 5 px width in both the radial and axial directions. The PDFs are ordered such that the lowest profile corresponds to $x/D_j = 0.2$ and the other profiles are shifted by a factor of 10 for better clarity. Also presented is the Gaussian fit for zero mean and the corresponding standard deviation. Mostly symmetric distributions are shown with wide tails, however the axial acceleration on the lip line near the jet exit shows asymmetry. At $x/D_j = 4$ for the radial locations $y/D_j = 0$ and 1, the distributions of acceleration are fairly isotropic, symmetric and match the Gaussian fit well over the centre peak but have wide tails. At the lip line the distributions deviate from the Gaussian fit, with a higher peak and a wider tail, that widens with axial distance. The radial location of $y/D_j = 1$ is in the quiescent region for the first two axial locations, and follows the Gaussian fit closely, however at $x/D_j = 4$, which is located in the outer shear layer, the PDF shows a wider tail.

4. CONCLUSIONS

Acceleration measurements were performed on a subsonic jet using four-pulse STB. High resolution instantaneous results and flow statistics are presented, for the first time revealing 3D acceleration and fluctuation fields, as well as PDF statistics. In the shear layer near the nozzle exit extremely high accelerations were measured. Cylindrical bin-averaging allowed sub-pixel (0.75 px or 23 μm) resolution flow statistics that appear to resolve the steep shear layer velocity gradients well.

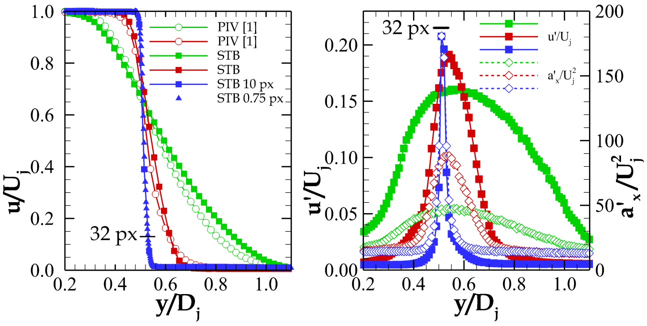

Figure 5: Velocity profiles of STB and PIV (left) and STB measured fluctuations of velocity and acceleration (right) at $x/D_j = 0.2$ (blue), 1 (red), 4 (green).

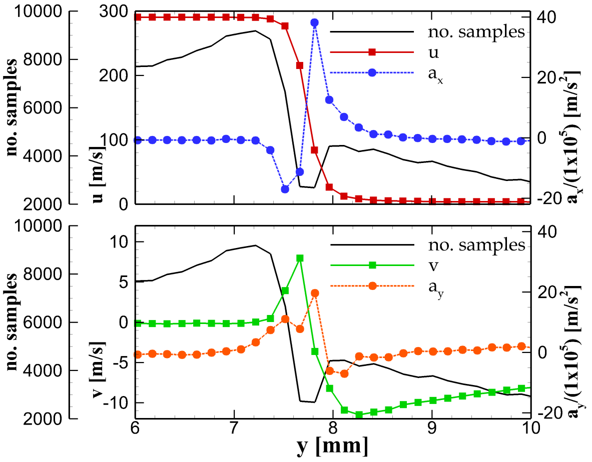

Figure 6: Axial (top) and radial (bottom), velocities and accelerations with the number of samples at $x/D_j = 0.2$.

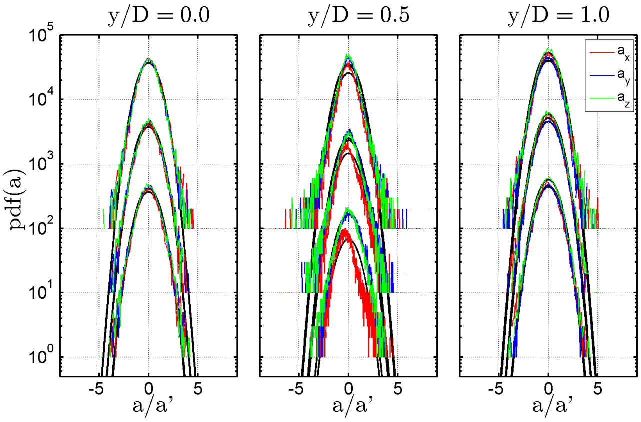

Figure 7: PDFs of the mean axial, a_x (red), radial, a_y (blue), out-of-plane, a_z (green) accelerations at radial locations.

REFERENCES

[1] Bridges, J. and Wernet, M., (2011), The NASA subsonic jet PIV dataset, *NASA/TM-2011-216807*.

[2] Kähler, C. J. and Kompenhans, J., (2000), Fundamentals of multiple plane stereo PIV, *Exp. in Fluids*, **29**.

[3] Novara, M., Schanz, D., Reuther, N., Kähler, C. J. and Schröder, A., (2016), LPT in high-speed flows: Shake-the-box for multi-pulse systems, *Exp. in Fluids*, **57**.

[4] Novara, M. *et al.*, (2016), LPT for multi-pulse systems: performance assessment, *In: 18th Int. Symp. on App. of Laser Tech. to Fluid Mech., Lisbon*.

[5] Perret, L. *et al.*, (2006), 3-Component acceleration field measurement by dual-time SPIV, *Exp. in Fluids*, **40**.

[6] Schanz, D., Gesemann, S. and Schröder, A., (2016), Shake-the-box: Lagrangian particle tracking at high particle image densities, *Exp. in Fluids*, **57**.

[7] Schröder, A. *et al.*, (2013), Dual volume and 4-pulse tomo-PIV using polarized laser light, *10th IS-PIV, Delft*.

[8] van Gent, P. L. *et al.*, (2017), Comparison of pressure field reconstructions from PIV and LPT, *Exp. in Fluids*, **58**.

[9] van Oudheusden, B., (2013), PIV-based pressure measurement, *Meas. Sci. and Tech.*, **24**.

[10] Wieneke, B., (2013), Iterative reconstruction of volumetric particle distribution, *Meas. Sci. and Tech.*, **24**.